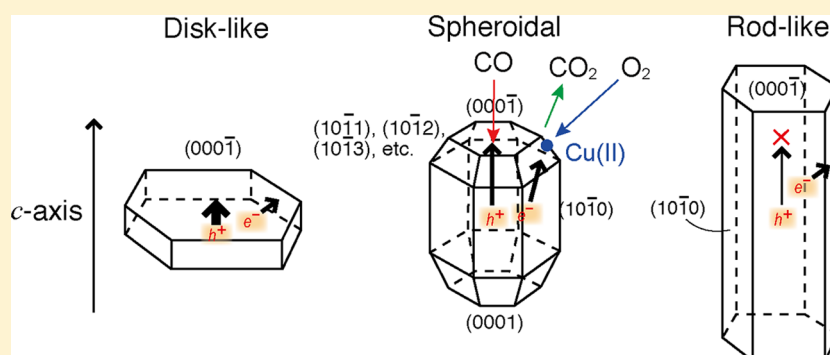


Preferential Photooxidation of CO in Hydrogen across the Crystalline Face Boundary over Spheroidal ZnO Promoted by Cu Ions

Yusuke Yoshida,[†] Takaomi Itoi,[‡] and Yasuo Izumi^{*,†}[†]Department of Chemistry, Graduate School of Science, Chiba University, Yayoi 1-33, Inage-ku, Chiba 263-8522, Japan[‡]Department of Mechanical Engineering, Graduate School of Engineering, Chiba University, Yayoi 1-33, Inage-ku, Chiba 263-8522, Japan

ABSTRACT: The design and synthesis of nanoscale zinc oxides (ZnOs) and their applications to photocatalysis are widely explored. However, the photocatalytic controls needed to design appropriate crystalline faces and promoter sites for each catalytic reaction step using ZnO have been rarely reported. This study optimized photocatalytic hydrogen purification using the preferential oxidation (PROX) of CO impurities among nanoscale disk-like, spheroidal, and rod-like ZnO promoted by adsorbed Cu ions. Four key factors were examined: (1) the diffusion length to the surface of separated electrons and holes induced by light; (2) the crystalline face where formate was formed from CO and its stability; (3) the crystalline face where Cu ions adsorbed for trapping electrons and reducing O₂; and (4) the frequency factor of “charge recombination as cations and anions” derived from photogenerated holes and electrons, respectively, at the boundary of crystalline faces. The optimal photocatalyst for hydrogen purification (CO PROX) was determined to be Cu-spheroidal ZnO. An efficient photocatalytic cycle was obtained by increasing the frequency factor between unstable unidentate formate on the (0001̄) face and Cu ions adsorbed on neighboring unsaturated {1011} faces.

1. INTRODUCTION

Various nanoparticles, nanotubes, and nanorods of zinc oxides have been extensively synthesized^{1–5} for potential applications in optical and electric materials,^{4,5} photovoltaics,^{6,7} and photocatalysts.⁸ The electric potentials at the bottom of the conduction band (CB) and at the top of the valence band (VB) of ZnO are similar to those of TiO₂; therefore, the band gap values are also similar (in the range of 3.0–3.2 eV).^{7,9} In contrast to utilizing the strong photooxidation power of TiO₂, the possibility of selective photooxidation utilizing the strong photooxidation power of ZnO is not well recognized.

Recently, spheroidal ZnO with an average major axis of 47 nm and an average minor axis of 22 nm was preferably grown in the direction of the [0 0 0 1] axis of wurtzite. The spheroidal ZnO with 0.5 wt % of adsorbed Cu²⁺ ions preferentially photooxidized 9700 ppm of CO to 0.35 ppm in 6.3 kPa of H₂ in 5 h.¹⁰ The achieved concentration of CO satisfied the regulation for the use of H₂ in fuel cells. The photocatalytic role of Cu ions was suggested to be as a photogenerated electron trap that provides electrons to the O₂ and/or O₂-derived intermediate species. Unlike in the proposed preferential

oxidation (PROX) mechanism in which CO adsorbs on metal nanoparticles (e.g., Au on TiO₂) and reacts with O₂ at the boundary between metal nanoparticles and the support,^{11,12} formate species were produced via eq 1:^{10,12}



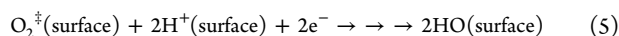
To complete the photocatalytic cycle, protons derived from one-electron-oxidized formate species eqs 2 and 3) must transfer and combine with the O₂-derived species to restore hydroxy groups (eqs 4 and 5):



Received: July 27, 2015

Revised: August 31, 2015

Published: August 31, 2015



In this study, disk-like, spheroidal, and rod-like ZnO nanoparticles were systematically synthesized to evaluate the geometric effects on the photo-PROX reaction of CO. Under light irradiation, charge separation occurs, and the charges diffuse to the surface. The diffusion lengths toward the polar (0 0 0 1) and (0 0 0 $\bar{1}$) faces are shorter for the disk-like and spheroidal ZnO, while the diffusion lengths toward the nonpolar {10 $\bar{1}$ 0} faces are shorter for spheroidal and rod-like ZnO (see table of contents graphic). To evaluate the diffusion efficiency, the electron diffusion toward adsorbed Cu²⁺ sites was monitored by X-ray absorption near-edge structure (XANES). The production of unstable intermediate formate species via eq 1 was followed by Fourier transform infrared (FTIR) spectroscopy.

Furthermore, the population of adsorbed Cu ions on each spheroidal ZnO face was investigated using high-resolution (HR) transmission electron microscopy (TEM) equipped with energy dispersive spectroscopy (EDS) to compare the elemental mappings of Cu K α and Zn K α . Furthermore, the interaction of O₂ with under-coordinated ZnO surfaces was simulated by the reductive precipitation of Ag⁺ ions via irradiation with ultraviolet (UV)–visible light over such surfaces and monitored by TEM.

The major finding of this study was that spheroidal ZnO was the best photo-PROX catalyst due to (1) the shorter photogenerated hole diffusion toward the unstable formate species that were dominant on the (0 0 0 $\bar{1}$) face; (2) the shorter photogenerated electron diffusion toward adsorbed Cu²⁺ and/or O₂-derived species on the under-coordinated faces of ZnO (e.g., {10 $\bar{1}$ 1}); and (3) the minimal distance between formate species and under-coordinated faces of ZnO.

2. EXPERIMENTAL SECTION

2.1. Photocatalyst Preparation. Disk-like ZnO was synthesized via the procedure reported in ref 13. Briefly, 2.0 mmol of zinc nitrate hexahydrate (>99.9%, Wako Pure Chemical), 10 mmol of urea (>99%, Wako Pure Chemical), 10 mmol of cetyltrimethylammonium bromide (>98%, Wako Pure Chemical), and 5.0 mL of 1-butanol (>99%, Wako Pure Chemical) were dissolved in 50 mL of deionized water (<0.06 $\mu\text{S cm}^{-1}$). This solution was stirred for 2 h at 290 K and then transferred into a Teflon-lined autoclave (TVS-N2-100, Taiatsu Techno; inner volume 100 mL) and kept at 393 K for 15 h. The solution was then cooled to 290 K, and the obtained white powder was filtrated using a 0.2- μm -pore polytetrafluoroethylene membrane filter (Omnipore JGWP04700, Millipore) and washed several times with deionized water (total 500 mL) and ethanol (total 300 mL). The powder was calcined at 573 K for 5 h. The obtained powder was denoted as disk-like ZnO.

The synthetic procedures for the spheroidal and rod-like ZnO were previously reported in ref 10. Briefly, zinc acetate dihydrate (11.6 g; purity >99%, Wako Pure Chemical) was suspended in ethanol (110 mL). A 0.50 M sodium hydroxide ethanol solution (50 mL; purity >97%, Kanto Chemical) was added to the Zn²⁺ solution and agitated using ultrasound (430 W, 38 kHz). The mixed suspension was refluxed at 353 K for 72 h. The obtained white precipitate was filtered using JGWP04700, washed with deionized water, and dried at 333 K for 12 h. The obtained white powder was denoted as spheroidal ZnO. Separately, a 0.20 M aqueous solution of Zn

sulfate heptahydrate (30 mL; purity >99.5%, Kanto Chemical) was added to 1.33 M NaOH aqueous solution (90 mL). The suspension was maintained at 333 K for 2 h. The white precipitate was filtered using JGWP04700, washed with deionized water, and dried at 333 K for 12 h. The obtained white powder was denoted as rod-like ZnO.

Cu ions were adsorbed on disk-like, spheroidal, or rod-like ZnO by mixing 0.150 g of ZnO with 0.40 mM Cu nitrate aqueous solution (30 mL; purity >99.9%, Wako Pure Chemical) for 30 min, filtrating using JGWP04700, washing with deionized water (total 100 mL), and drying at 333 K for 8 h. The obtained powder samples were denoted as Cu-disk-like ZnO, Cu-spheroidal ZnO, and Cu-rod-like ZnO; the corresponding Cu uptake values were 100, 100, and 64% (0.50, 0.50, and 0.32 wt %), respectively, based on the X-ray absorbance (the edge jump values in XANES). The Cu content was typically 0.50 wt % for Cu-disk-like ZnO and Cu-spheroidal ZnO, but samples containing 0.10 wt % were also prepared by mixing 0.150 g of spheroidal ZnO with 0.080 mM Cu nitrate aqueous solution (30 mL).

The photoreduction of Ag⁺ ions using the Cu-spheroidal ZnO sample was monitored by photodeposition from the aqueous Ag nitrate solution. Ag nitrate (1.0 mg, > 99.8%, Wako Pure Chemical) was dissolved in 30 mL of deionized water, and 0.1 mL of ethanol and 50 mg of Cu-spheroidal ZnO were added to the solution. The suspension was irradiated from above by UV–visible light from a 300-W xenon arc lamp (model OPM2-500XQ, Ushio) for 10 min. The distance between the exit of the lamp house and the surface of the suspension was 40 cm. The suspension was then filtrated using a JGWP04700 filter, washed with 100 mL of deionized water, and dried at 290 K for 72 h. A grayish blue powder was obtained for TEM observation.

2.2. Photocatalyst Characterization. Nitrogen adsorption isotherm measurements were performed at 77 K in the pressure range of 1.0–90 kPa in a vacuum system connected to diffusion and rotary pumps (10⁻⁶ Pa) and equipped with a capacitance manometer (Models CCMT-1000A and GM-2001, ULVAC). The Brunauer–Emmett–Teller (BET) surface area (S_{BET}) was calculated using eight-point measurements between 10 and 46 kPa ($P/P_0 = 0.10$ – 0.45) in the adsorption isotherm. The samples (40–200 mg) were evacuated, and the temperature was elevated at a rate of 4 K min⁻¹ to 393 K and maintained at 393 K for 2 h before the measurements.

Scanning electron microscopy (SEM) images were observed using a model JSM-6510A (JEOL) at the Center for Analytical Instrumentation, Chiba University. A tungsten filament was used in the electron gun and the electron accelerating voltage was 15 kV. TEM images were obtained using a model H-7650 (Hitachi). The samples were mounted on Cu mesh (150 mesh per inch) coated with a copolymer film of poly(vinyl alcohol) and formaldehyde (Formvar, Monsanto) and coated with carbon. A tungsten filament was used in the electron gun, and the electron accelerating voltage was 100 kV. The magnification ranged between 60000 \times and 600000 \times . High-angle annular dark field (HAADF) scanning TEM (STEM) and HR-TEM images were also observed using a model JEM-2100F (JEOL). Chemical compositions and elemental distributions were analyzed with EDS using a Si(Li) detector equipped in the TEM. X-ray diffraction (XRD) patterns were observed using a D8 ADVANCE diffractometer (Bruker) and a Mini-Flex diffractometer (Rigaku).

Table 1. Structural Data for ZnO and ZnO with Adsorbed Cu

entry	sample	Cu		average particle size (nm)			XRD peak ratio (10 $\bar{1}$ 0):(0002):(10 $\bar{1}$ 1)
		wt %	S_{BET} ($\text{m}^2 \text{g}^{-1}$)	t^b	t_{major}	t_{minor}	
A	disk-like ZnO	0	75	24	1700	20	100:81:156
B	spheroidal ZnO	0	35	39	47	22	100:121:189
C	rod-like ZnO	0	20	48	440	80	100:115:181
D	FZO-50 ^a	0	50	21	20	20	100:93:175
E	Cu-disk-like ZnO	0.50	47				
F	Cu-spheroidal ZnO	0.50	39	34	35	24	100:96:192
G	Cu-rod-like ZnO	0.32	32				

^aZnO > 97.4%, Ishihara Sangyo Co. ^bBased on Scherrer equation $t = 0.9\lambda/(\text{peak width} \times \cos \theta_{\text{Bragg}})$ for (10 $\bar{1}$ 1) peak.

UV–visible and FTIR spectra were measured using a model V-650 (JASCO) spectrophotometer equipped with an integrating sphere (ISV-469, JASCO) for diffuse reflectance measurements in the wavelength region between 200 and 800 nm and a model FT/IR-4200 spectrophotometer equipped with a mercury–cadmium–tellurium-M detector (JASCO) in the wavenumber region between 4000 and 650 cm^{-1} , respectively. For the FTIR measurements, the energy resolution was set to 2 cm^{-1} . A photocatalyst sample disk ($\phi = 20$ mm, 35–150 mg) was positioned perpendicular to the IR beam in a quartz reactor equipped with transparent NaCl windows on both sides and connected to a vacuum system (10^{-6} Pa). First, the sample disk was evacuated for 2 h at 290 K in the reactor, and then 4.6 kPa of CO was introduced.

Cu K-edge X-ray absorption fine structure (XAFS) spectra were measured at 290 K on beamlines NW10A and 9C in the transmission mode at the Photon Factory Advanced Ring (PFAR) and Photon Factory (PF) at the High Energy Accelerator Research Organization (Tsukuba). Si(3 1 1) and Si(1 1 1) double-crystal monochromators were inserted in the X-ray beam path. The storage ring energy and ring current at PFAR were 6.5 GeV and 50 mA, respectively; at PF, the respective values were 2.5 GeV and 450 mA. The X-ray intensity was maintained at 65% of the maximum flux using a Piezo translator set on the crystal. The slit opening size in front of the I_0 ionization chamber was 1 mm (vertical) \times 2 mm (horizontal). The I_0 and I_{transmit} ionization chambers (Oken) were purged with N_2 and a gas mixture of N_2 (85%) + Ar (15%), respectively.

The sample disk was set in a Pyrex glass cell equipped with a 25- μm -thick polyethylene naphthalate window (Q51-25, Teijin). The sample was vertically positioned at the center between the exit window of the I_0 ionization chamber and the entrance window of the I_{transmit} ionization chamber and tilted to make the X-ray incident angle to the sample surface equal to 45°. The sample was illuminated with an Xe arc lamp (500 W; model UI-502Q, Ushio) placed perpendicular to the X-ray beam path in the same horizontal plane with initial CO , O_2 , and H_2 pressures of 46 Pa, 92 Pa, and 4.5 kPa, respectively. During the irradiation, a shoulder peak intensity at 8983.1 eV gradually grew. The Cu^{I} site ratio was evaluated from a linear approximation of peak intensity at 8983.1 eV for Cu^{II} and Cu^{I} sites based on eq 6:

$$\text{Cu}^{\text{I}} - \text{site ratio} \approx \frac{\text{peak intensity@8983.1eV} - 0.048(\text{for Cu}^{\text{II}} 100\%)}{0.21(\text{for Cu}^{\text{I}} 100\%) - 0.048(\text{for Cu}^{\text{II}} 100\%)} \quad (6)$$

Thus, the photoreduction rates of Cu^{II} sites in the three ZnO samples were evaluated. A control experiment was performed separately for a sample under argon at atmospheric pressure. The distance between the center of the sample and the exit window of the lamp house (Model UI-502Q) was 42 mm. The scan steps were ~ 9 , ~ 0.3 , and ~ 2.5 eV in the pre-edge, edge, and postedge regions, respectively. The data accumulation time was 1.0 s for each data point. The Cu K-edge absorption energy value was calibrated to 8980.3 eV for the spectrum of Cu metal.^{14,15} The energy position of the monochromator was reproduced within ± 0.1 eV.

The XAFS data were analyzed using an XDAP package.¹⁶ The pre-edge background was approximated by the modified Victoreen function $(C_2/E^2) + (C_1/E) + C_0$. The background of postedge oscillation was approximated by a smoothing spline function calculated using eq 7 for the number of data points:

$$\sum_{i=1}^{\text{data points}} \frac{(\mu x_i - \text{BG}_i)^2}{\exp(-0.075k_i^2)} \leq \text{smoothing factor} \quad (7)$$

where k is the wavenumber of the photoelectrons.

Multiple-shell curve-fit analyses were performed for the Fourier-filtered k^3 -weighted extended XAFS (EXAFS) data in both k - and R -space using empirical amplitude and phase-shift parameters extracted from the EXAFS data for CuO . The interatomic distances (R) and the associated coordination numbers (N) for the Cu–O and Cu(–O–)Cu pairs were set to an R value of 0.1956 nm with an N value of 4 and to an R value of 0.3028 nm with an N value of 10, respectively, on the basis of their crystal structures.¹⁷ The σ^2 value was referenced to the model parameter ($\Delta\sigma^2$). The many-body reduction factor S_0^2 was assumed to be equal for both the sample and the reference.

2.3. Photo-PROX Reaction Tests. The photo-PROX reaction of CO in predominant hydrogen was performed in a closed circulating system equipped with a quartz reactor comprising 23.8 cm^2 of the flat bottom section.^{18–22} The total internal volume of the system was 143 mL. Photocatalyst powder (50 mg) was homogeneously spread at the bottom of the reactor and evacuated (10^{-6} Pa) for 2 h prior to the photocatalytic test, and reaction gas (H_2 370 μmol ; CO 3.7 μmol ; O_2 4.5 μmol) was introduced. The photocatalyst was irradiated by UV–visible light from a 500-W xenon arc lamp (UI-502Q). The distance between the exit of the lamp house and the photocatalyst was 24 cm, and the light intensity at the center of the photocatalyst was 42 mW cm^{-2} . The products and reactants were analyzed using columns of 13X-S molecular sieve and polyethylene glycol (PEG)-6000 supported on Flusin P (GL Sciences) set in the online gas chromatograph equipped with a thermal conductivity detector (Shimadzu, model GC-

8A). The photocatalytic activity (in units of mol) was evaluated based on eqs 8 and 9:

$$\text{CO conversion}(\%) = 100 \times (n_{\text{CO},0\text{h}} - n_{\text{CO},3\text{h}}) / n_{\text{CO},0\text{h}} \quad (8)$$

$$\text{Selectivity}(\%) = 100 \times n_{\text{CO}_2} / (n_{\text{CO}_2} + n_{\text{H}_2\text{O}}) \quad (9)$$

Furthermore, first-order reactions were assumed (eq 10), and the rate constants were evaluated by the fit to eq 11:

$$-\frac{dP_{\text{CO},t}}{dt} = k(P_{\text{CO},t} - P_{\text{CO},\text{final}}) \quad (10)$$

The differential eq 10 is solved by integration

$$\frac{P_{\text{CO},t} - P_{\text{CO},\text{final}}}{P_{\text{CO},\text{initial}} - P_{\text{CO},\text{final}}} = e^{-kt} \quad (11)$$

3. RESULTS

3.1. SEM and XRD Characterization. The obtained spheroidal and rod-like ZnO crystallites were anisotropic with mean sizes of $47 \text{ nm} \times 22 \text{ nm}$ and $440 \text{ nm} \times 80 \text{ nm}$, respectively (Table 1B,C).¹⁰ In contrast, based on the SEM image (Figure 1A), the synthesized disk-like ZnO consisted of nanoplates with a mean thickness of 20 nm and a mean diameter of $1.7 \mu\text{m}$ (Table 1A).

Three XRD peaks appeared in the $2\theta_{\text{B}}$ range (θ_{B} : Bragg angle) of 29° – 39° for disk-like, spheroidal, and rod-like ZnO; these peaks were assigned to the $10\bar{1}0$, 0002 , and $10\bar{1}1$ reflections of wurtzite ZnO (Figure 2a–c), respectively. Among the three peaks for disk-like ZnO grown in the direction perpendicular to the c -axis, the 0002 peak intensity was weaker than the intensities of the $10\bar{1}0$ and $10\bar{1}1$ peaks (Figure 2a, Table 1A). The $10\bar{1}1$ reflection was the most intense among the three peaks, especially for spheroidal, rod-like, and FZO-50 ZnO (Table 1B–D). The $10\bar{1}1$ reflection was even more intense for Cu-spheroidal ZnO than that for spheroidal ZnO (Table 1B, F).

3.2. Monitoring of Distribution of Adsorbed Cu Ions and Photoreduction Sites via Ag^+ Precipitation. The distribution of Cu ions adsorbed on spheroidal ZnO was observed by HAADF-STEM and elemental mapping using EDS (Figure 3A). In the HAADF-STEM image of Cu-spheroidal ZnO, spheroidal particles with sizes of 16–38 nm in the direction of major axis and 7.6–21 nm in the direction of minor axis were observed. The Zn $K\alpha$, Cu $K\alpha$, and O $K\alpha$ mappings distributed in the upper left region, similar to in the HAADF-STEM image of Cu-spheroidal ZnO (Figure 3A).

The ED spectra of a $\sim 5 \text{ nm}$ selected area for Cu-spheroidal ZnO (red circle: edge; blue circle: center; and green circle: edge on the other side for spheroids) were also measured (Figure 3B). The Cu $K\alpha$ and Zn $K\alpha$ intensities were compared among the selected areas on the spheroidal ZnO. It should be noted that the Cu $K\alpha$ peak appeared at 8.0 keV in the blank test in the absence of sample due to the Cu mesh of the sample mount (Figure 3B, top right). Therefore, the Cu $K\alpha$ peak intensity for the blank test was subtracted from the Cu $K\alpha$ peak intensity for the Cu-spheroidal ZnO sample. After this adjustment, the peak ratio of (Cu $K\alpha$)/(Zn $K\alpha$) at the edge of Cu-spheroidal ZnO was 0.44 ± 0.15 (Figure 3B, red and green circles), whereas the ratio at the center of Cu-spheroidal ZnO was 0.32 ± 0.06 (Figure 3B, blue circle). Taking error into

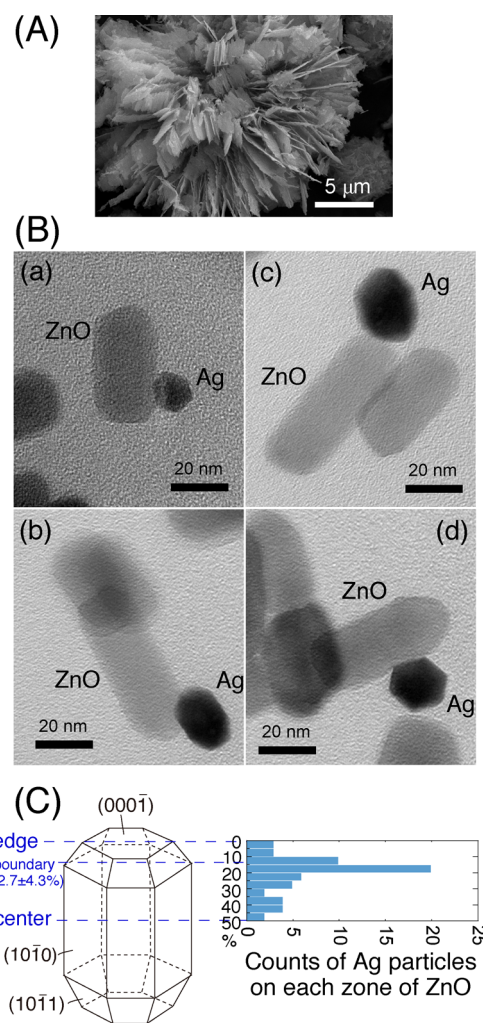


Figure 1. (A) SEM image of disk-like ZnO. (B) TEM images of minimal uptake of Ag^+ ion on Cu-spheroidal ZnO [(a)–(d)] by UV-visible irradiation for 10 min. (C) Histogram of the population of photodeposited Ag particles on each zone of spheroidal ZnO from the edge to center.

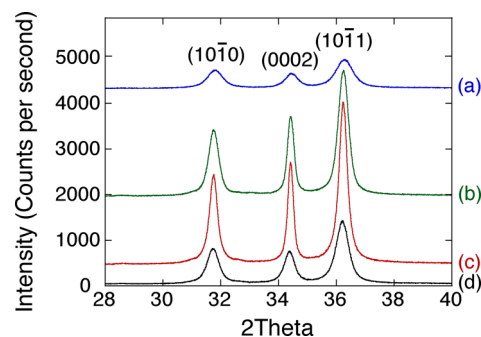


Figure 2. XRD patterns of disk-like ZnO (a), spheroidal ZnO (b), rod-like ZnO (c), and FZO-50 (d).

account, the peak ratio of (Cu $K\alpha$)/(Zn $K\alpha$) is greater at the edge than at the center.

Minimal uptake of Ag^+ ions on Cu-spheroidal ZnO under the irradiation of UV-visible light was monitored by TEM (Figure 1B). In average for the ZnO spheroids, the zone from the edge to $12.7(\pm 4.3)\%$ was $\{10\bar{1}1\}$ planes and that from $12.7(\pm 4.3)\%$ to the center (50%) was $\{10\bar{1}0\}$ planes. In the image, the

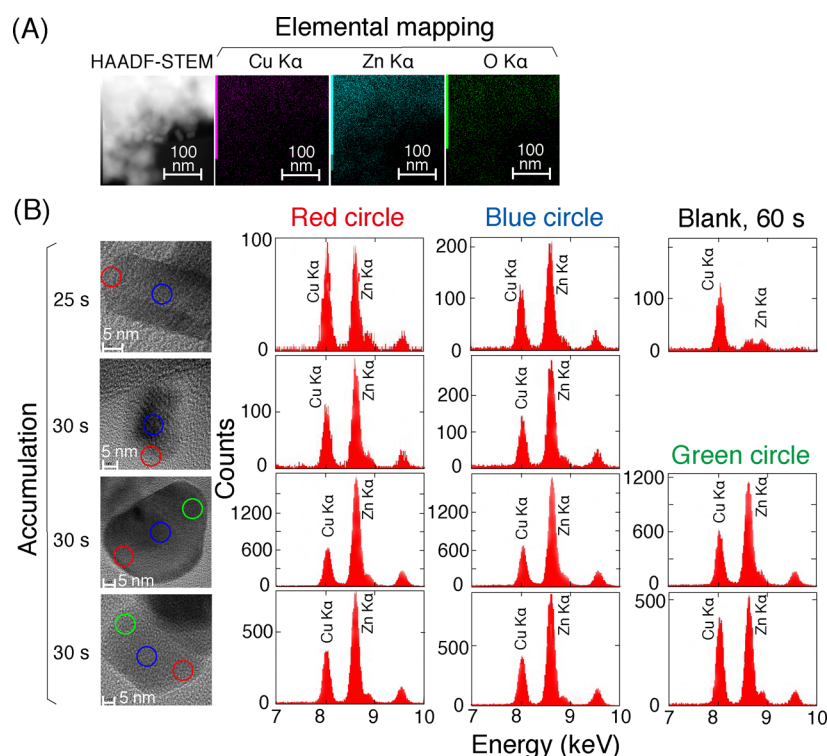


Figure 3. (A) HAADF-STEM image and the elemental mappings for Cu K α , Zn K α , and O K α in the same view as the HAADF-STEM image for Cu-spheroidal ZnO. (B) HR-TEM images and EDS spectra for a \sim 5 nm selected area (red, blue, and green circles) of Cu-spheroidal ZnO.

deposited Ag⁰ nanoparticles populated mostly on {10 $\bar{1}$ 1} slopes and also at the boundary between slopes of the {10 $\bar{1}$ 1} and {10 $\bar{1}$ 0} planes and the population gradually decreased to the center of ZnO spheroids (see the histogram in Figure 1C). These results suggest that the preferable reduction sites of Ag⁺ were on the unsaturated interface sites between the {10 $\bar{1}$ 1} and {10 $\bar{1}$ 0} planes and/or relatively unsaturated {10 $\bar{1}$ 1} plane compared to {10 $\bar{1}$ 0} planes.

3.3. FTIR Spectra of the Three ZnOs in CO. CO gas (4.6 kPa) was introduced into the ZnO (Figure 4) to clearly monitor the adsorbed species. 4.6 kPa corresponded to by 100 times greater than the CO pressure (46 Pa) for the photo-PROX reaction tests in this study. When 46 Pa of CO was introduced to ZnO, it was difficult to quantitatively determine the surface species due to the background modulation resulting from the amount change of Zn carbonate at the surface.

After 1 h of CO introduction, peaks appeared at 1629, 1604, 1397, and 1342 cm⁻¹ in the spectrum of disk-like ZnO (Figure 4A1), at 1641 and 1605 cm⁻¹ in the spectrum of spheroidal ZnO (Figure 4C1), and at 1638, 1606, and 1393 cm⁻¹ in the spectrum of rod-like ZnO (Figure 4E1) in the wavenumber range of 1700–1300 cm⁻¹. Based on the spectra, these peaks were assigned to two types of surface formate species including Cu-ZnOs. Subsequently, the CO gas was evacuated (Figure 4A2–F2). The intercorrelated peaks appearing at 1649–1620 cm⁻¹ and 1442–1393 cm⁻¹ were assigned to the antisymmetric [$\nu_{as}(\text{OCO})$] and symmetric stretching vibration [$\nu_s(\text{OCO})$] of formate “Species A”. The other intercorrelated peaks appearing at 1606–1592 cm⁻¹ and 1361–1342 cm⁻¹ were assigned to the antisymmetric [$\nu_{as}(\text{OCO})$] and symmetric stretching vibration [$\nu_s(\text{OCO})$] of formate “Species B”. The background was not always sufficiently flat due to the effects of residual carbonate species adsorbed on basic ZnO (not shown).

Species A and B were formed on ZnO via the adsorption of CO gas. No significant differences were observed between the intensities of Species A and/or B for each sample per sample amount (100 mg) at 0.023–0.030 for $\nu_{as}(\text{OCO})$ and 0.024–0.045 for $\nu_s(\text{OCO})$. After the evacuation of CO gas, Species A and B decreased/disappeared in the spectra of all the ZnO samples (Figure 4A2, C2, E2). For disk-like and rod-like ZnO, only Species A remained, and its intensity decreased to 5%–40% and to 48%–56%, respectively, of the intensity under CO. Conversely, 63% of Species A and 61% of Species B remained in the case of spheroidal ZnO.

3.4. FTIR Spectra for Three Cu-ZnOs in CO. Surface formate Species A and B were also confirmed in Cu-ZnO samples in 4.6 kPa of CO, and the $\nu_{as}(\text{OCO})$ peak intensities per sample amount compared to the corresponding peak for ZnO under CO increased by 1.5–2.8 times because of the effects of the Cu ions (Table 2).

In Cu-disk-like ZnO, the peaks at 1642 and 1400 cm⁻¹ were assigned as Species A; their intensities decreased by 20%–79% of those under CO after the removal of CO gas (Figure 4B1, 2). Species B was not clearly observed/resolved.

In Cu-spheroidal ZnO under CO, Species A appeared at 1643 and 1442 cm⁻¹, and Species B appeared at 1602 and 1361 cm⁻¹ (Figure 4D1). In addition, the peak due to Cu¹⁺-CO appeared at 2090 cm⁻¹. After the evacuation of CO gas, 56%–74% of the peaks due to Species B remained, in clear contrast to Species A, which totally disappeared (Figure 4D2). The spectrum in Figure 4D2 taken under dark did not change significantly if the Cu-spheroidal ZnO sample disk was irradiated by UV–visible light. Because the signal/background ratio became worse if the samples were irradiated by UV–visible light, FTIR spectra taken only under dark were shown in this study. As the trend for Species A was not observed for spheroidal ZnO, the added Cu ions destabilized Species A.

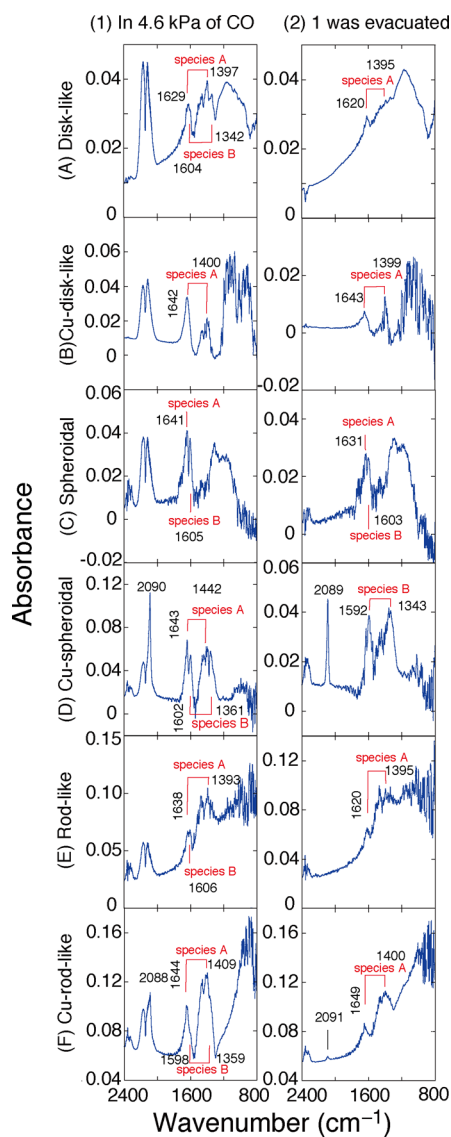


Figure 4. FTIR spectra under dark of disk-like ZnO (A), Cu-disk-like ZnO (B), spheroidal ZnO (C), Cu-spheroidal ZnO (D), rod-like ZnO (E), and Cu-rod-like ZnO (F). The conditions are under 4.6 kPa of CO for 1 h (1) and the sample from 1 after being evacuated for 10 min (2).

In the case of Cu-rod-like ZnO under CO, Species A appeared at 1644 and 1409 cm^{-1} , while the shoulder peaks of Species B appeared at 1598 and 1359 cm^{-1} (Figure 4F1). As for the Cu-spheroidal ZnO, a $\text{Cu}^{\text{I}}\text{-CO}$ peak was observed at 2088 cm^{-1} . In addition, 24%–39% of the peaks due to Species A remained after the evacuation of CO gas, whereas Species B disappeared (Figure 4F2).

The stabilities of Species A and B under vacuum were different in each sample. Species A was unstable on spheroidal ZnO, especially Cu ions-adsorbed ZnO. In contrast, Species B was stable on spheroidal ZnO, likely on the (10 $\bar{1}$ 1) face, because of the different exposed crystal faces. Species A was relatively stable on Cu-disk-like ZnO and Cu-rod-like ZnO; however, its peak intensity was weak.

3.5. Monitoring of Cu Valence State by XANES. The photoreduction rates of Cu sites were compared among Cu-disk-like ZnO, Cu-spheroidal ZnO, and Cu-rod-like ZnO irradiated by UV-visible light under 46 Pa of CO, 92 Pa of O₂,

and 4.5 kPa of H₂. Prior to the irradiation, a tiny 1s-3d quadrupole-transition pre-edge peak appeared at 8978.3–8978.6 eV for all the samples (Figure 5B-a, a'), indicating that the Cu valence state was II for all the incipient samples. The 1s-3d pre-edge peak intensity and a shoulder peak at 8983.1 eV for as-prepared Cu-spheroidal ZnO negligibly changed if the sample was evacuated at 290 K for 2 h (Figure 5A2a, a'; B2a, a'), demonstrating that evacuation effects on the Cu state were negligible. During 55 min of irradiation, the pre-edge peak intensity decreased and a shoulder peak at 8983.1 eV gradually grew for all the Cu-ZnOs. The Cu^I site ratio was evaluated based on eq 6 (see the Experimental Section). Assuming first-order reaction kinetics for the reduction ($[\text{Cu}^{\text{II}}] = [\text{Cu}^{\text{II}}]_{\text{initial}} e^{-k_{\text{Cu reduction}} t}$), the rate constant $k_{\text{Cu reduction}}$ was determined to be 0.0082, 0.0076, and 0.0032 min^{-1} for Cu-disk-like ZnO, Cu-spheroidal ZnO, and Cu-rod-like ZnO, respectively (Table 3E, G, H).

As a control test, the reduction of Cu^{II} sites was also monitored for Cu-spheroidal ZnO under Ar gas and UV-visible irradiation. The reduction of Cu^{II} sites was not clear, and the k value was determined to be below the detection limit ($<0.0005 \text{ min}^{-1}$), which was significantly smaller than that under the mixed reaction gas of CO, O₂, and H₂ (0.0076 min^{-1} ; Table 3G). Thus, the presence of CO and/or H₂ as a reducing reagent was the requisite for charge separation in Cu-ZnO samples and the reduction of Cu^{II} to Cu^I.

3.6. Determination of Site Structure by EXAFS Spectra. The Cu K-edge EXAFS spectra were measured for the Cu-spheroidal ZnO photocatalyst freshly evacuated at 290 K for 2 h (Figure 6A) and for the sample under CO (46 Pa), O₂ (92 Pa), and H₂ (4.5 kPa) for 55 min irradiated with an Xe arc lamp (Figure 6B). Based on the curve-fit analyses, the first-shell coordination distances of the Cu–O interatomic pair were 0.1922 nm with an N value of 3.7 for the fresh sample in darkness (Table 4 and Figures 6A3, 4) and 0.195 nm with an N value of 3.2 for the sample tested photocatalytically for 55 min (Table 4 and Figures 6B3, 4).

The second-shell coordination of the Cu(–O–)Zn interatomic pair was not clearly observed in the Fourier transform for the fresh sample (Figure 6A2). In contrast, a weak peak at 0.27 nm (phase-shift uncorrected; Figure 6B2) was nicely fit at 0.300 nm with an N value of 2.4 as Cu(–O–)Zn interatomic pair for the Cu-spheroidal ZnO subjected to the photo-PROX test with CO for 55 min (Table 4 and Figure 6B3, 4). No peaks associated with the metallic Cu–Cu interatomic pair at ~ 0.256 nm appeared in the spectra of either sample (Figure 6A2, B2).

For Cu-disk-like ZnO, the interatomic distance of the Cu–O pair was 0.193 nm with an N value of 4.3 for the fresh sample. The data negligibly changed to 0.194 nm with an N value of 3.8 for the sample after photocatalytic test for 55 min. The Cu(–O–)Zn coordination was significant only for sample after photocatalytic test (at 0.3176 nm with the N value of 3.2), similar to the data for Cu-spheroidal ZnO (Table 4).

For Cu-rod-like ZnO, the $R(\text{Cu-O})$ value was slightly longer: 0.1952 nm with an N value of 3.2 for the fresh sample. The data negligibly changed to 0.1957 nm with an N value of 3.6 for the sample after photocatalytic test for 55 min. The Cu(–O–)Zn coordination was not significant both before and after photocatalytic test (Table 4). In summary, the Cu–O interatomic pair at 0.1922–0.1957 nm with the N values of 3.2–4.3 for Cu-ZnOs in this study suggested major CuO-like coordination [$N(\text{Cu-O}) = 4$; Table 4] rather than Cu₂O-like coordination [$N(\text{Cu-O}) = 2$].

Table 2. Wavenumber and Intensity of FTIR Peaks for Disk-Like, Spheroidal, and Rod-Like ZnOs and Cu-Supported ZnOs with CO and Reference Samples under Various Conditions

entry	gas (pressure)	peaks (cm ⁻¹)						assignment	ref
		(peak height)							
		$\nu_{as}(\text{OCO})$ + $\delta(\text{CH})$	$\nu(\text{CH})$	$\nu_s(\text{OCO})$ + $\delta(\text{CH})$	$\nu(\text{CO})$	$\nu_{as}(\text{OCO})$	$\nu_s(\text{OCO})$		
(A) disk-like ZnO ^a									
1	CO (4.6 kPa)					1629, (0.025) (1604)	1397, (0.040) 1342 (0.024)	Species A Species B	this work
2	1 was evacuated					1620 (0.010)	1395 (0.002)	Species A	
(B) Cu-disk-like ZnO (0.5 wt % Cu) ^a									
1	CO (4.6 kPa)					1642 (0.069)	1400 (0.066)	Species A	this work
2	1 was evacuated					1643 (0.014)	1399 (0.052)	Species A	
(C) spheroidal ZnO ^b									
1	CO (4.6 kPa)					1641, (0.030) 1605 (0.023)		Species A Species B	this work
2	1 was evacuated					1631 (0.019) 1603 (0.014)		Species A Species B	
(D) Cu-spheroidal ZnO (0.5 wt % Cu) ^b									
1	CO (4.6 kPa)				2090 (0.052)	1643, (0.046) 1602 (0.035)	1442, (0.039) 1361 (0.039)	Species A Species B	this work
2	1 was evacuated	2930 (0.005)	2857 (0.004)		2089 (0.028)	1592 (0.026)	1343 (0.022)	Species B	
(E) rod-like ZnO ^c									
1	CO (4.6 kPa)					1638, (0.025) 1606 (0.024)	1393 (0.045)	Species A Species B	this work
2	1 was evacuated					1620 (0.012)	1395 (0.025)	Species A	
(F) Cu-rod-like ZnO (0.5 wt % Cu) ^c									
1	CO (4.6 kPa)				2088 (0.020)	1644, (0.062) 1598 (0.008)	1409, (0.085) 1359 (0.007)	Species A Species B	this work
2	1 was evacuated				2091 (0.004)	1649 (0.015)	1400 (0.033)	Species A	
(G) ZnO									
1	HCO ₂ H	2960				1580	1365	Species B	26
(H) ZnO/SiO ₂									
1	HCO ₂ H					1625, 1587	1374	Species B	27
2	acetaldehyde					1602	1372	Species B	27
(I) Cu/SiO ₂									
1	HCO ₂ H	2939	2859			1558	1359	Species B on Cu	28
(J) Cu/ZnO/SiO ₂									
1	HCO ₂ H	2939	2897, 2858			1626, 1582	1360	Species B	27
2	acetaldehyde	2969, 2936	2900, 2857			1595, 1626,	1385,	Species B on Zn	27

Table 2. continued

entry	gas (pressure)	peaks (cm^{-1})						assignment	ref
		(peak height)							
		$\nu_{\text{as}}(\text{OCO})$		$\nu_{\text{s}}(\text{OCO})$		$\nu_{\text{as}}(\text{OCO})$	$\nu_{\text{s}}(\text{OCO})$		
		$+\delta(\text{CH})$	$\nu(\text{CH})$	$+\delta(\text{CH})$	$\nu(\text{CO})$				
(K) Cu/ZnO						1557	1358	Species B on Cu	
1	$\text{CO}_2 + \text{H}_2$ (1:9) (101 kPa)	2970	2880	2740		1580	1365	Species B	24

^{a,b,c}Peak height is converted value if 100 mg of photocatalyst sample is used (35–40 mg,^a 120–150 mg,^b and 60–120 mg^c used in measurements).

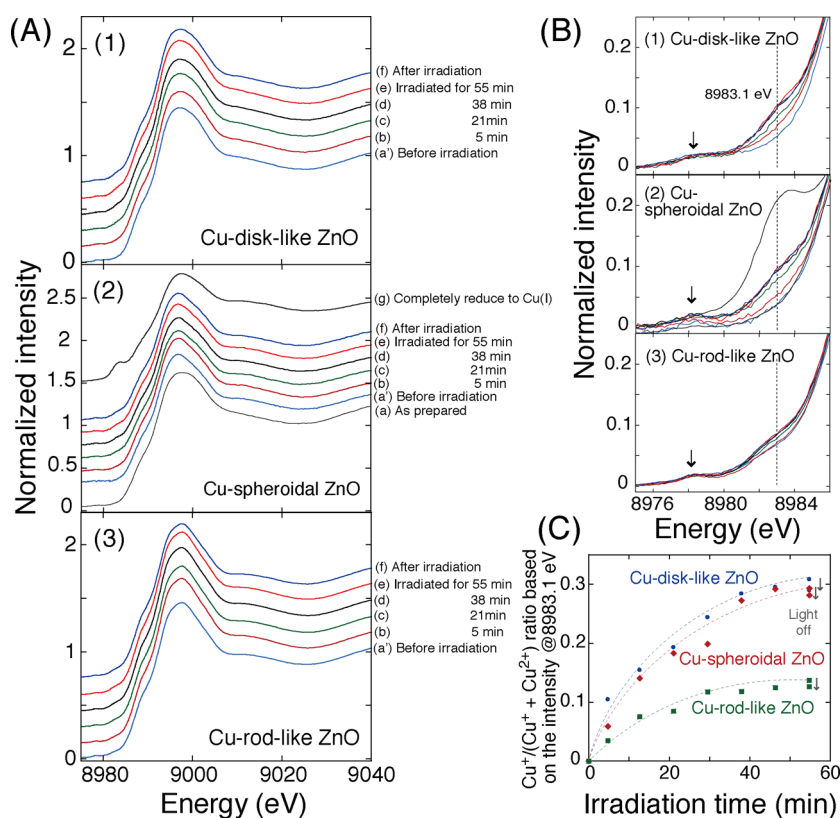


Figure 5. (A) Normalized Cu K-edge XANES for Cu-disk-like (1), Cu-spheroidal (2), and Cu-rod-like ZnO (3) as prepared (a), evacuated at 290 K for 2 h before irradiation (a'), at 5 min (b), 21 min (c), 38 min (d), and 55 min (e) from the start of UV–visible light irradiation from a 500-W Xe arc lamp with the initial pressures of CO (46 Pa), O_2 (92 Pa), and H_2 (4.5 kPa), at 1 min after irradiation (f), and completely reduced Cu^1 -spheroidal ZnO (g). (B) Expanded view of the pre-edge region in panel A. (C) The intensity change in the shoulder peak at 8983.1 eV during irradiation by UV–visible light for Cu-disk-like (\bullet), Cu-spheroidal (\blacklozenge), and Cu-rod-like ZnOs (\blacksquare).

Table 3. Results of Photo-PROX Reactions for 55 min^a and the Reduction Rates of Cu Ion Sites for Irradiation under CO , O_2 , and H_2

entry	photocatalysts	Cu wt %	1st order		CO		CO		Quantum		1st order		ref.
			k_{PROX} (10^{-3} min^{-1})	removal rate ^b ($\mu\text{mol h}^{-1} \text{ g}_{\text{cat}}^{-1}$)	conv. ^c (%)	Selec. ^d (%)	efficiency (%)	$k_{\text{Cu reduction}}$ (10^{-3} min^{-1})					
A	disk-like ZnO	0	6.0	28	59	98	0.017						
B	spheroidal ZnO	0	4.3	25	57	97	0.015					10	
C	rod-like ZnO	0	0.1	2.4	2.3	51	0.001					10	
D	FZO-50	0	4.4	29	57	96	0.018					10	
E	Cu-disk-like ZnO	0.50	17	59	91	99	0.036			8.2			
F	Cu-spheroidal ZnO	0.10	31	97	97	96	0.059					10	
G		0.50	25	82	97	99	0.050			7.6			
H	Cu-rod-like ZnO	0.32	2.1	16	30	100	0.010			3.2			

^a H_2 6.4 kPa, CO 64 Pa, and O_2 76 Pa. ^bIn 0.5 h of reaction. ^cConversion. ^dSelectivity.

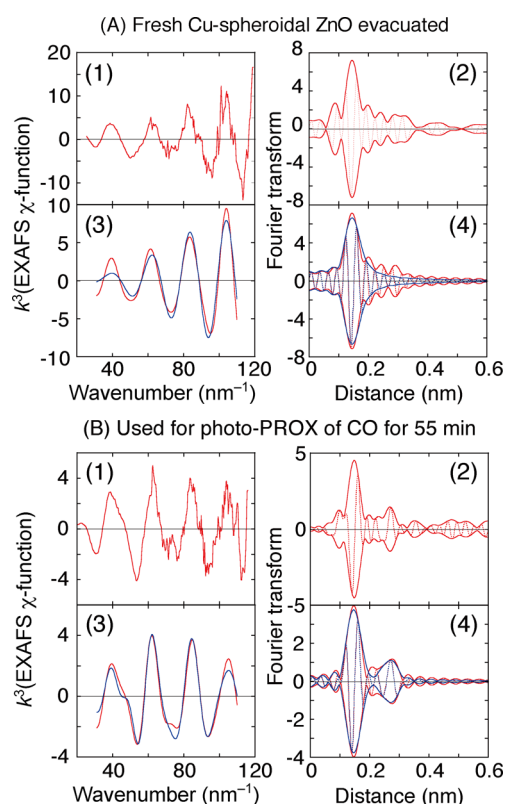


Figure 6. Cu K-edge EXAFS spectra for Cu-spheroidal ZnO (0.5 wt % Cu): (A) a fresh sample evacuated at 290 K for 2 h; and (B) a sample in CO (46 Pa) + O₂ (92 Pa) + H₂ (4.5 kPa) irradiated with UV-visible light for 55 min. (1) The k^3 -weighted EXAFS χ -function, (2) its associated Fourier transform, and (3, 4) the best-fit results in (3) k -space and (4) R -space. The thin red lines represent the experimental values, and the thick blue lines represent the calculated values in panels (3) and (4). The solid lines represent the magnitude, and the dotted lines (---) represent the imaginary part in panels (2) and (4).

3.7. Photo-PROX Tests Using the ZnOs and Cu-ZnOs.

In photo-PROX reaction tests among ZnOs, the CO removal

rate and conversion decreased in the following order (Table 3A–D):

$$\begin{aligned} &\text{disk-like ZnO} > \text{FZO} - 50 \\ &> \text{spheroidal ZnO} \\ &\gg \text{rod-like ZnO} \end{aligned} \quad (12)$$

For disk-like ZnO, a shorter crystalline growth length in the c -direction (Table 1, t_{minor}) corresponded to a better photo-PROX performance, suggesting the importance of photo-generated charge diffusion in the c -direction of wurtzite-type ZnO. In the time course using ZnOs (Figure 7A–C), the amount of decrease in CO nearly corresponded to amount of CO₂ formation. However, the decreases in the amounts of CO and O₂ were nearly equivalent, with the exception of in rod-like ZnO (even more excess of O₂ decrease) despite the 2:1 reaction stoichiometry (2CO + O₂ → 2CO₂), suggesting that O₂ was adsorbed on the ZnO surface.

When Cu was loaded over various ZnOs, the CO removal rates and conversions were enhanced by Cu and decreased in the following order (Table 3E–H):

$$\begin{aligned} &\text{Cu-spheroidal ZnO (0.10 wt \% Cu)} \\ &> \text{Cu-spheroidal ZnO (0.50 wt \% Cu)} \\ &> \text{Cu-disk-like ZnO} \\ &\gg \text{Cu-rod-like ZnO} \end{aligned} \quad (13)$$

The selectivity toward CO₂ was not complete using ZnOs: 51–98% (Table 3A–D) and in fact minor water was formed using spheroidal and rod-like ZnOs (Figures 7B, C). In contrast, the CO photo-PROX selectivity was improved to be higher than 96% for all the Cu-ZnO photocatalysts (Table 3E–H). The stoichiometry of the reaction (2CO + O₂ → 2CO₂) was preserved in the time course of Cu-ZnOs (Figures 7D–F), with the exception of the latter part of reaction test for Cu-spheroidal ZnO because CO was almost consumed after 1.5 h (Figure 7E).¹⁰

Table 4. Best-Fit Results of Cu K-Edge EXAFS Analyses for Cu-ZnOs^a

sample	Cu–O			Cu(–O–)M (M = Zn, Cu)			goodness of fit	ref
	N	R (nm)	$\Delta\sigma^2$ (10 ^{–5} nm ²)	N	R (nm)	$\Delta\sigma^2$ (10 ^{–5} nm ²)		
Cu-disk-like ZnO, fresh	4.3 (±1.2)	0.193 (±0.001)	5.4 (±4.9)				1000	this work
used ^b	3.8 (±1.0)	0.194 (±0.001)	4.0 (±4.4)	3.2 (±0.6)	0.3176 (±0.0004)	6.1 (±3.2)	150	this work
Cu-spheroidal ZnO, fresh	3.7 (±0.4)	0.1922 (±0.0004)	–3.8 (±0.6)				1600	this work
used ^b	3.2 (±0.5)	0.195 (±0.001)	–1.2 (±1.3)	2.4 (±0.3)	0.300 (±0.001)	–4.5 (±2.1)	200	this work
Cu-rod-like ZnO, fresh	3.2 (±0.3)	0.1952 (±0.0004)	–0.4 (±0.9)				1000	this work
used ^b	3.6 (±0.4)	0.1957 (±0.0005)	0.7 (±1.1)				400	this work
CuO	4	0.1956		10	0.3028			17
Cu ₂ O	2	0.18488		12	0.30191			17

^aThe values in parenthesis are fit errors. ^bAfter photocatalysis in CO (46 Pa) + O₂ (92 Pa) + H₂ (4.5 kPa) for 55 min.

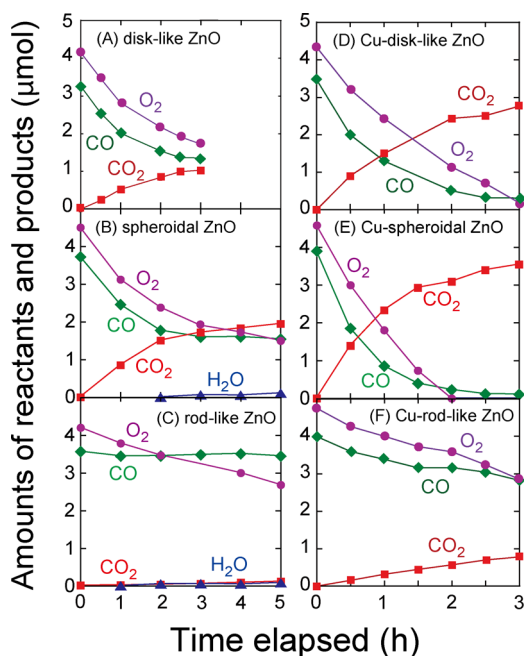
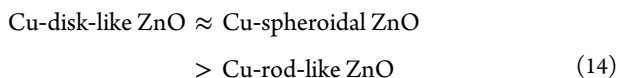


Figure 7. Time course of the PROX reaction of CO in H₂ using disk-like ZnO (A), spheroidal ZnO (B),¹⁰ rod-like ZnO (C),¹⁰ Cu-disk-like ZnO (D), Cu-spheroidal ZnO (E),¹⁰ and Cu-rod-like ZnO (F) illuminated with UV–visible light. Reaction gases: CO 3.7 μmol (63 Pa), H₂ 370 μmol (6.3 kPa), and O₂ 4.5 μmol (76 Pa).

4. DISCUSSION

4.1. Photogenerated Electron Diffusion. Based on the growth of the shoulder peak at 8983.1 eV in the in situ XANES spectra (Figure 5), the photoreduction rates of Cu^{II} sites in the three ZnO samples followed the order (Table 3):

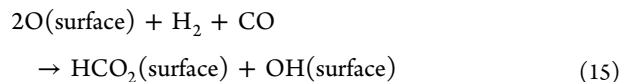


The thin ZnO disks (mean thickness = 20 nm) of the Cu-disk-like ZnO and nanocrystallites of the Cu-spheroidal ZnO (mean major axis 35 nm × minor axis 24 nm; Table 1F) were apparently advantageous for the diffusion of photogenerated electrons from bulk to surface Cu sites. The difference in charge diffusion path length is the major reason for the poor photocatalytic activity obtained using Cu-rod-like ZnO.

The diffusion path of photogenerated electrons from bulk to surface was visualized using TEM as the reductive photo-deposition of Ag nanoparticles on Cu-spheroidal ZnO sample starting from Ag⁺ ions (Figure 1B). As compared to the zones of edge, {10 $\bar{1}$ 1} faces, and {10 $\bar{1}$ 0} faces in ZnO spheroids (Figure 1C), the Ag nanoparticles populated mostly near the boundary between slopes of the {10 $\bar{1}$ 1} and {10 $\bar{1}$ 0} faces and on {10 $\bar{1}$ 1} faces, suggesting that these relatively unsaturated zones on ZnO spheroids on each end are the key photo-reduction sites for Ag⁺ and possibly for O₂. The population of deposited Ag nanoparticles gradually decreased to the center of ZnO spheroids probably because a part of photoreduced Ag nanoparticles on unsaturated zones noted above diffused to {10 $\bar{1}$ 0} planes and stabilized (Figure 1B, C).

4.2. Assignments of Formate Species. In the FTIR spectrum for Cu-supported ZnO in CO₂ + H₂,^{23,24} the absorption peaks of formate species at 1580 and 1365 cm⁻¹ were assigned to ν_{as}(OCO) and ν_s(OCO), respectively (Table

2K). Formate species are widely accepted to be the reaction intermediate in the synthesis of methanol from CO (and/or CO₂) and hydrogen over Cu-ZnO catalysts via eq 15:²⁵



The ν_{as}(OCO) and ν_s(OCO) peaks were within/very near the wavenumber range for formate Species B observed under 4.6 kPa of CO: ν_{as}(OCO) at 1606–1592 cm⁻¹ and ν_s(OCO) at 1361–1342 cm⁻¹ (Table 2). Species B was also reported as ν_{as}(OCO) between 1587 and 1558 cm⁻¹ and ν_s(OCO) between 1374 and 1359 cm⁻¹ for ZnO,²⁶ ZnO/SiO₂,²⁷ Cu/SiO₂,²⁸ and Cu/ZnO/SiO₂²⁷ in gaseous formic acid (Table 2G–J), respectively. In the literature,^{25–28} Species B is considered to be bridging formate (Scheme 1A2). The minor difference in ν_{as}(OCO) wavenumber in this study compared to those in refs 26–28 can be attributed to the different surface; the surface hydroxy group to react with CO in this study versus the surface consisted of Zn-terminating sites and O-terminating site to react dissociatively with HC(=O)O–H.^{26–28}

A pair of Species B peaks was observed at 1602 and 1361 cm⁻¹ for Cu-spheroidal ZnO in 4.6 kPa of CO (Figure 4D1 and Table 2D1). The two peaks remained at 1592 and 1343 cm⁻¹ in vacuum (Figure 4D2 and Table 2D2). In contrast, another pair of peaks corresponding to Species A was observed at 1643 and 1442 cm⁻¹ in 4.6 kPa of CO and totally disappeared in vacuum.

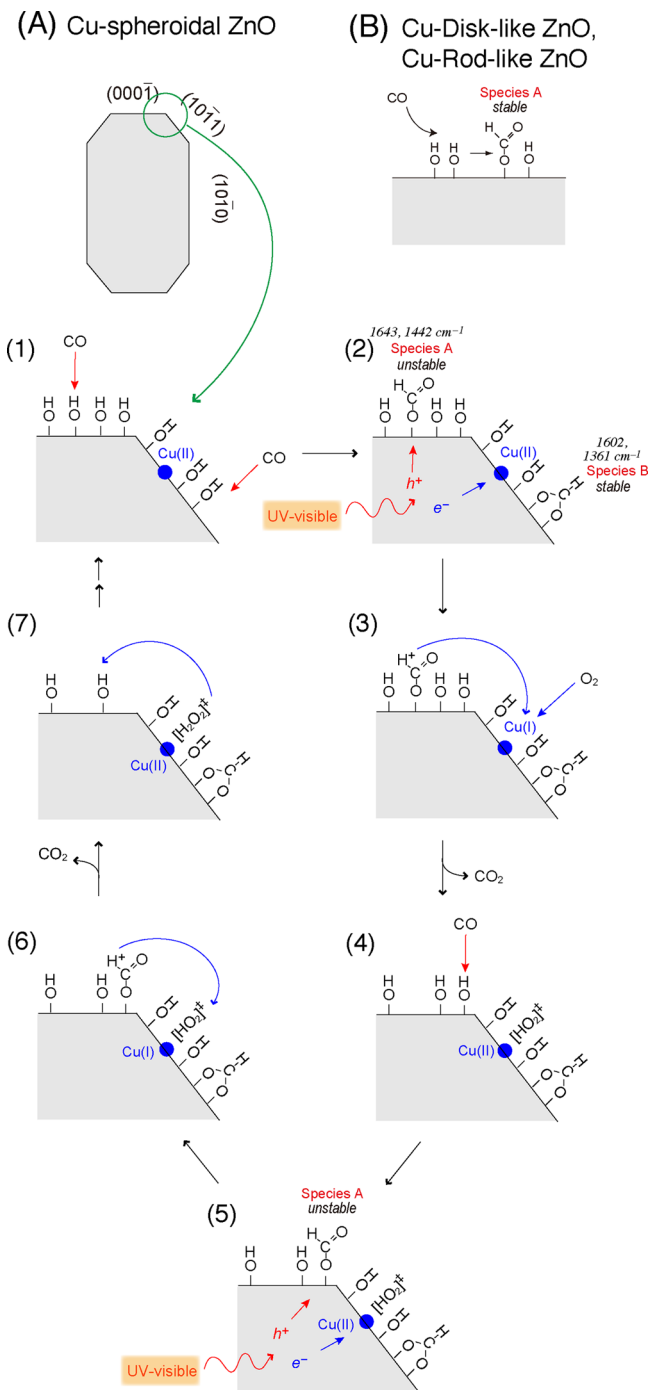
The ν_{as}(OCO) and ν_s(OCO) peaks for formate Species A under 4.6 kPa of CO ranged from 1649 to 1620 cm⁻¹ and 1442–1393 cm⁻¹, respectively (Table 2). Species A was unstable or totally disappeared under vacuum for Cu-spheroidal ZnO. Compared to the relatively stable Species B, Species A can be considered as unidentate formate (Scheme 1A2). The preferable formation of unidentate formate on the ZnO (0 0 0 $\bar{1}$) face has been reported.^{23,24}

Under CO gas, the formate Species A was formed by the reaction of CO molecules with surface hydroxy groups (i.e., the ZnO (000 $\bar{1}$) face on disk-like and rod-like ZnO), whereas formic acid dissociatively adsorbs as Species A onto Zn-terminating surface sites (i.e., the ZnO (0001) face)²⁹ or onto Cu ions over the ZnO surface. Thus, Species A was formed via the dissociative adsorption of formic acid on surface Zn and O ions to form Zn–O–C(=O)H and hydroxy species, whereas CO inserted into surface hydroxy groups under CO. This chemical difference led to the different populations of Species A derived from CO and formic acid.

The ν_{as}(OCO) and ν_s(OCO) peak intensities associated with Species A and B for spheroidal ZnO (0.014–0.030) were 54%–66% (adjusted for sample weight) of that of corresponding peaks for Cu-spheroidal ZnO when the samples were under 4.6 kPa of CO (Figure 4D1, C1) or when the gaseous CO was evacuated (Figure 4D2, C2). Therefore, half as much formate species should be formed on or assisted by the Cu-ion sites for Cu-spheroidal ZnO.

In the comparison of total ν_{as}(OCO) and ν_s(OCO) peak intensities associated with Species A and B in 4.6 kPa of CO or after the evacuation, no clear trend was found among disk-like, spheroidal, and rod-like ZnOs (total peak intensity: 0.053–0.094 in CO and 0.012–0.037 after evacuation; Table 2A, C, E) and among Cu-disk-like ZnO, Cu-spheroidal ZnO, and rod-like ZnO (total peak intensity: 0.135–0.162 in CO and 0.048–0.066 after evacuation; Table 2B, D, F). The total peak

Scheme 1. Proposed Surface Reaction Steps for the Photo-PROX Reaction of CO in Hydrogen Gas via Formate Species A and the Route to Accumulate Inactive Formate Species B for Cu-ZnOs



intensities did not correlate to the CO photo-PROX activity order (Table 3, eqs 12 and 13). Conversely, species B appeared only for spheroidal ZnO and Cu-spheroidal ZnO after evacuation of CO (Table 2C2, D2) among all samples measured for Figure 4. Thus, the preference to Species B and destabilization of Species A by added Cu (Table 2C2, D2) should be closely related to the best CO photo-PROX performance using Cu-spheroidal ZnO.

It should be noted that the formates (and CO) adsorbed on Cu ions (Figure 4) cannot be the intermediate in the CO

oxidation reaction because Cu ions serve as electron traps and donor, as demonstrated by XANES, Ag^+ photodeposition, and HR-TEM combined with elemental mapping. Furthermore, no reduced products from CO, e.g., formaldehyde, methanol, or methane, were detected in this study. Thus, the relatively unstable Species A formed on the Zn sites by the CO insertion into surface hydroxy groups under CO is the potential intermediate to photooxidation to CO_2 . The well-satisfied, polar (000 $\bar{1}$) face should be favorable to form Species A on Zn (Scheme 1A1).

4.3. Coordination and Distribution of Adsorbed Cu Sites. In the Fourier transform of the Cu K-edge EXAFS spectrum of the fresh Cu-spheroidal ZnO evacuated for 2 h (Figure 6A2), only the Cu–O interatomic pair was observed, and the N value was 3.7 based on the curve-fit analysis. The XANES spectra (pre-edge peak at 8978.3–8978.6 eV and a shoulder peak at 8983.1 eV) for as-prepared Cu-spheroidal ZnO negligibly changed if the sample was evacuated for 2 h at 290 K (Figure 5A2a, a'; B2a, a'). Thus, the Cu sites were exclusively in the valence II under these conditions.¹⁰

The N values for Cu–O for the fresh Cu-ZnOs were 4.3–3.2 similar to 4 for CuO (Table 3). Slightly lower N value for fresh Cu-rod-like ZnO (3.2) should be due to desorption of adsorbed water, O_2 , or CO_2 by evacuation at 290 K. The $N(\text{Cu–O})$ value of 3 was reported for Cu-ZnO^{10,30,31} and CuO–ZnO/ Al_2O_3 .³²

After the sample was irradiated with UV–visible light for 55 min (Figure 6B2), the interatomic distance of Cu–O changed negligibly from 0.1922 to 0.195 nm. The N value for Cu–O slightly decreased to 3.2, and the Cu(O–)Zn pair was observed at 0.300 nm based on the curve-fit analysis. No metallic Cu–Cu bond(s) was observed throughout this study (Table 4). As evaluated by XANES (Figure 5), 31% of Cu^{II} sites in fresh Cu-spheroidal ZnO was reduced to Cu^{I} after photocatalytic test for 55 min. Thus, theoretical N value for Cu–O pair in Cu-spheroidal ZnO after photocatalytic test would be $4 \times 0.69 + 2 \times 0.31 = 3.38$,¹⁷ almost in agreement with the experimental $N(\text{Cu–O})$ value of 3.2 (Table 4). The photoreduction to Cu^{I} in $\text{CO} + \text{O}_2 + \text{H}_2$ (0.0076 min^{-1} ; Table 3G) negligibly proceeded under Ar ($<0.0005 \text{ min}^{-1}$), demonstrating the reduction proceeded, e.g.



It should be noted that the amount of Cu^{I} sites was monitored (Figure 5) in the dynamic equilibrium of CO photo-PROX irradiated by UV–visible light (Scheme 1A). The reduction rates monitored in Figure 5C would be for Cu^{I} sites that did not quickly reoxidize for the O_2 reduction (Scheme 1A4, 7).¹⁰

The HR-TEM results and elemental mapping using Cu $K\alpha$ (Figure 3B) indicated that Cu^{II} ions were well dispersed on spheroidal ZnO. As a result, more Cu was populated on the edge region of the spheroid (i.e., (000 $\bar{1}$) and {10 $\bar{1}$ 1}) than in the central region of the spheroid. In relation to the Cu distribution, photodeposition sites for Ag^+ were observed predominantly on {10 $\bar{1}$ 1} faces and the interface to {10 $\bar{1}$ 0} faces. Thus, Cu ions preferably adsorb on the unsaturated {10 $\bar{1}$ 1} faces of spheroidal ZnO during catalyst preparation and serve as electron trap sites for Ag^+ ions. Furthermore, the charges generated by light irradiation in nanospheroidal ZnO easily reached the {10 $\bar{1}$ 1} face with a relatively shorter diffusion length. The mean size of ZnO spheroids was 47 nm \times 39 nm

(ZnO) or 35 nm × 24 nm (Cu-ZnO), by far shorter compared to the reported electron diffusion length of 50–140 μm.³³

Conversely, Cu sites also interacted with CO. Cu^I sites formed by the desorption of the surface O atoms of spherical ZnO adsorbed CO, as evidenced by an FTIR peak at 2090–2089 cm⁻¹ (Figure 4D). The O vacancy on ZnO was reported in vacuum at 433 K³⁴ and in helium at 513–533 K.³⁵ Owing to the presence of reducible Cu^{II} sites over ZnO surface, formed O vacancy in vacuum at 290 K should result in the Cu^I–CO peak in this study. The O vacancy formation on Cu-ZnO in vacuum was also reported, but at 873 K.³⁶ As discussed above based on Figure 5A2a, a'; B2a, a', predominant Cu sites in Cu-spheroidal ZnO were valence II before the photocatalytic tests. Furthermore, no reduced products from CO were detected in this study. Conversely, we did not detect any Cu⁰ sites in XANES (Figure 5) and EXAFS (Figure 6) after CO photo-PROX tests that are plausible if Cu^I–CO species was the intermediate to CO₂. Furthermore, no Cu^I–CO peak was observed for decently active Cu-disk-like ZnO (Table 3E) under CO + O₂ + H₂ and UV–visible light, like Figure 4A2, in contrast that weak Cu^I–CO peak appeared for quite poor Cu-rod-like ZnO under the conditions, like Figure 4F2. Thus, the Cu^I–CO species were inert not to participate in catalysis and the Cu^I sites need to be free for the coordination of O₂ (Scheme 1A3) to work as reduction sites.

The FTIR peak intensity [$\nu_{as}(\text{OCO})$, $\nu_s(\text{OCO})$] due to formate Species A and B increased by 1.5–1.9 times after the addition of 0.5 wt % Cu to spherical ZnO (Table 2). We suspect that the formate Species A (unidentate) was mainly associated with Cu (Figure 4D1) and unstable in vacuum (Figure 4D2). The preferable Cu distribution on edge regions (i.e., {000 $\bar{1}$ } and {10 $\bar{1}$ 1}) rather than in the center (Figure 3B) along with the preferable population of unstable Species A on the well-satisfied, polar {000 $\bar{1}$ } face are the key factors in converting CO to CO₂ during the photo-PROX reaction (Scheme 1A1, 2).

4.4. Proposed CO PROX Reaction Mechanism. The following photo-PROX reaction steps are proposed: formate Species A is formed³⁷ (Scheme 1A1 → 2; 4 → 5; eq 1) and oxidized by photogenerated holes (Scheme 1A2 → 3; 5 → 6; eq 2); surface Cu²⁺ sites, which populate preferably on unsaturated edge sites of spherical ZnO, e.g., {10 $\bar{1}$ 1} faces, are reduced by photogenerated electrons (2 → 3; 5 → 6);¹⁰ and O₂ is reduced by electrons via Cu-ion trapping sites coupled with protons of oxidized formate species H⁺CO₂ across the crystalline face boundary (3 → 4 → 5 → 6 → 7) to regenerate two surface hydroxy groups (Scheme 1A7 → 1; eq 5). The separation of photooxidation and photoreduction sites was reported depending on the crystal face (e.g., {0 0 1} and {1 0 1}) of TiO₂.^{38–41} In the case of Cu-spheroidal ZnO, we suspect that the Species A on the {000 $\bar{1}$ } face and Cu sites on the {10 $\bar{1}$ 1} face should be very close, enabling proton transfer (Scheme 1A3 and 6) and hydroxy restoration (7 → 1). In a context that a proton transfer controlled the catalysis, this proposed mechanism including proton transfer from formate species is closely related to CO PROX mechanism on Au/TiO₂ catalyst, whereas proton transfer from carboxy intermediate on Au was proposed in ref 12. Although following eq 17 is four-electron process



reaction mechanism proposed in Scheme 1 proceeds by two photons to form two pairs of electrons and holes utilizing

hydroxy groups eqs 1–5. Thus, the quantum efficiency of this reaction was calculated to 0.059% for Cu-spheroidal ZnO (Table 3F). It should be noted ~81% of incident UV–visible light was transmitted through the photocatalyst under the conditions of CO PROX tests in this study,¹⁰ and the effective quantum efficiency would be 0.31% for Cu-spheroidal ZnO. Species B should be accumulated (Scheme 1A2) and eventually become inert.

The CO removal rate and rate constant k_{PROX} for Cu-spheroidal ZnO (97 μmol h⁻¹ g_{cat}⁻¹ and 0.031 min⁻¹) could not reach the values using Au-TiO₂ (1200 μmol h⁻¹ g_{cat}⁻¹ and 0.141 min⁻¹) by 12–4.5 times under similar reaction conditions (11 mg, 290 K, initial pressure H₂ 6.3 kPa, CO 63 Pa, O₂ 150 Pa, no light),¹ but the k_{PROX} for Cu-spheroidal ZnO was on the same order as the one for CuO/CeO₂⁴² (0.085 min⁻¹) under similar reaction conditions (50 mg, 323 K, initial pressure H₂ 6.3 kPa, CO 63 Pa, O₂ 76 Pa, no light).⁴³ The Cu-spheroidal ZnO photocatalysts sustainably substitute inexpensive Cu and Zn for Au^{11,12} or Ce⁴² under the condition that enough area is available for the irradiation of sunlight.

The photogenerated holes would not reach Species A (Scheme 1B) in rod-like ZnO (mean length = 440 nm and mean diameter = 80 nm; Table 1C) based on the hole diffusion length of 240–440 nm.^{44,45} The length in the [0 0 0 1] direction of the rods should limit the CO PROX activity for rod-like ZnO and Cu-rod-like ZnO (eqs 12 and 13).

Conversely, formate Species A were clearly observed for Cu-disk-like ZnO (Figure 4B), likely from the reaction of CO with the predominant {000 $\bar{1}$ } face. In fact, such Species A were suggested to be good intermediates to CO₂ in the CO photo-PROX reaction for ZnOs (eq 12). Cu (0.5 wt %) was also stably adsorbed on disk-like ZnO (Table 1E); however, Cu-disk-like ZnO was inferior to Cu-spheroidal ZnO in terms of CO photo-PROX activity (eq 13). One possible explanation is that the effective separation of photooxidation and photoreduction sites was difficult for Cu-disk-like ZnO compared to the photooxidation of Species A on the {000 $\bar{1}$ } face and the photoreduction of O₂ on Cu ions on the {10 $\bar{1}$ 1} faces for Cu-spheroidal ZnO (Scheme 1A).

5. CONCLUSIONS

The anisotropic effects of ZnO on the CO photo-PROX reaction using Cu-ZnO along with the distribution and the role of adsorbed Cu^{II} ions were investigated in this study. The order of CO photo-PROX activity was as follows: disk-like ZnO > spherical ZnO ≫ rod-like ZnO. Adsorbed Cu ions improved the photocatalytic performance in all ZnOs, and the new order of activity became Cu-spheroidal ZnO (0.10 wt % of Cu) > Cu-spheroidal ZnO (0.50 wt % of Cu) > Cu-disk-like ZnO ≫ Cu-rod-like ZnO. For comparison, the photogenerated electron transfer rates to surface Cu^{II} sites for Cu-ZnO were monitored using XANES and followed the order: Cu-disk-like ZnO ≈ Cu-spheroidal ZnO > Cu-rod-like ZnO.

The distributions of Cu²⁺ sites and reduction sites for Ag⁺ ions over spherical ZnO crystallites were investigated using elemental mapping and TEM. Cu²⁺ ions populated more at the edge regions rather than at the center regions of spheroids. EXAFS demonstrated that the Cu ions were atomically dispersed on ZnO. The Ag particles formed under irradiation with UV–visible light in the presence of ethanol deposited predominantly over the slope {10 $\bar{1}$ 1} faces and the interface to {10 $\bar{1}$ 0} faces of spherical ZnO crystallites. Thus, {10 $\bar{1}$ 1} faces were suggested to be the key photoreduction sites for O₂.

Conversely, two types of formate species were detected for ZnO and Cu-ZnO samples under CO gas using FTIR via the reaction of CO and surface hydroxy groups. Species A, which appeared at 1649–1620 cm^{-1} and 1442–1393 cm^{-1} , was relatively unstable and assigned to unidentate formate. Species B, which appeared at 1606–1592 cm^{-1} and 1361–1342 cm^{-1} , was assigned to bridging formate. The well-satisfied, polar (000 $\bar{1}$) face should be favorable to form unidentate formate on Zn.

A plausible reaction mechanism for the CO PROX reaction using the most efficient Cu-spheroidal ZnO photocatalyst was proposed as follows. Species A was formed on the (000 $\bar{1}$) face of spheroidal ZnO via the reaction between CO and surface hydroxy groups and oxidized by photogenerated holes. The surface Cu^{2+} sites, which formed preferably on the unsaturated {10 $\bar{1}$ 1} edge faces of spheroidal ZnO, trapped and donated photogenerated electrons to O_2 . Charge recombination between cations and anions then occurred via proton transfer from the oxidized formate species H^+CO_2^- to $[\text{O}_2^-]^{\ddagger}$ species near the boundary of the (000 $\bar{1}$) and {10 $\bar{1}$ 1} faces. One more proton transfer coupled to CO oxidation to $[\text{HO}_2^-]^{\ddagger}$ species would restore two hydroxy groups to complete a catalytic cycle (Scheme 1A).

AUTHOR INFORMATION

Corresponding Author

*E-mail: yizumi@faculty.chiba-u.jp. Fax: +81-43-290-2783.

Notes

The authors declare no competing financial interest.

ACKNOWLEDGMENTS

The authors are grateful for the financial support from the Grant-in-Aid for Scientific Research C (26410204 and 22550117) and the Research Fellowship for Young Scientists (25-489; Y.Y.) from the Japan Society for the Promotion of Science and approval of the Photon Factory Proposal Review Committee for X-ray measurements (2013G159 and 2011G083).

REFERENCES

- (1) Li, Y.; Yang, X. Y.; Feng, Y.; Yuan, Z. Y.; Su, B. L. One-Dimensional Metal Nanotubes, Nanowires, Nanoribbons, and Nanorods: Synthesis, Characterizations, Properties and Applications. *Crit. Rev. Solid State Mater. Sci.* **2012**, *37*, 1–74.
- (2) Catlow, C. R. A.; Bromley, S. T.; Hamad, S.; Mora-Fonz, M.; Sokol, A. A.; Woodley, S. M. Modelling Nano-Clusters and Nucleation. *Phys. Chem. Chem. Phys.* **2010**, *12*, 786–811.
- (3) Wang, Z. L. ZnO Nanowire and Nanobelt Platform for Nanotechnology. *Mater. Sci. Eng., R* **2009**, *64*, 33–71.
- (4) Wang, X.; Song, J.; Wang, Z. L. Nanowire and Nanobelt Arrays of Zinc Oxide from Synthesis to Properties and to Novel Devices. *J. Mater. Chem.* **2007**, *17*, 711–720.
- (5) Grätzel, M. Mesoporous Oxide Junctions and Nanostructured Solar Cells. *Curr. Opin. Colloid Interface Sci.* **1999**, *4*, 314–321.
- (6) Grätzel, M. Photoelectrochemical Cells. *Nature* **2001**, *414*, 338–344.
- (7) Hernández-Alonso, M. D.; Fresno, F.; Suárez, S.; Coronado, J. M. Development of Alternative Photocatalysts to TiO_2 : Challenges and Opportunities. *Energy Environ. Sci.* **2009**, *2*, 1231–1257.
- (8) Valdés, Á.; Qu, Z. W.; Kroes, G. J.; Rossmeißl, J.; Nørskov, J. K. Oxidation and Photo-Oxidation of Water on TiO_2 Surface. *J. Phys. Chem. C* **2008**, *112*, 9872–9879.
- (9) Chen, X.; Mao, S. S. Titanium Dioxide Nanomaterials: Synthesis, Properties, Modifications, and Applications. *Chem. Rev.* **2007**, *107*, 2891–2959.

- (10) Yoshida, Y.; Mitani, Y.; Itoi, T.; Izumi, Y. Preferential Oxidation of Carbon Monoxide in Hydrogen Using Zinc Oxide Photocatalysts Promoted and Tuned by Adsorbed Copper Ions. *J. Catal.* **2012**, *287*, 190–202.

- (11) Green, I. X.; Tang, W.; Neurock, M.; Yates, J. T., Jr. Spectroscopic Observation of Dual Catalytic Sites During Oxidation of CO on a Au/ TiO_2 Catalyst. *Science* **2011**, *333*, 736–739.

- (12) Saavedra, J.; Doan, H. A.; Pursell, C. J.; Grabow, L. C.; Chandler, B. D. The Critical Role of Water at the Gold-Titanium Interface in Catalytic CO Oxidation. *Science* **2014**, *345*, 1599–1602.

- (13) Zhou, X.; Hu, Z.; Fan, Y.; Chen, S.; Ding, W.; Xu, N. Microspheric Organization of Multilayered ZnO Nanosheets with Hierarchically Porous Structures. *J. Phys. Chem. C* **2008**, *112*, 11722–11728.

- (14) Bearden, J. A. X-Ray Wavelengths. *Rev. Mod. Phys.* **1967**, *39*, 78–124.

- (15) Zschornack, G. *Handbook of X-ray Data*; Springer: Berlin, 2007; p 233.

- (16) Vaarkamp, M.; Linders, H.; Koningsberger, D. *XDAP version 2.2.7*; XAFS Services International: Woudenberg, The Netherlands, 2006.

- (17) Hyde, B. G.; Andersson, S. *Inorganic Crystal Structures*; John Wiley & Sons: New York, 1989; p 12.

- (18) Ahmed, N.; Morikawa, M.; Izumi, Y. Photocatalytic Conversion of Carbon Dioxide into Methanol Using Optimized Layered Double Hydroxide Catalysts. *Catal. Today* **2012**, *185*, 263–269.

- (19) Ahmed, N.; Shibata, Y.; Taniguchi, T.; Izumi, Y. Photocatalytic Conversion of Carbon Dioxide into Methanol Using Zinc–Copper–M(III) (M = Aluminum, Gallium) Layered Double Hydroxides. *J. Catal.* **2011**, *279*, 123–135.

- (20) Izumi, Y.; Itoi, T.; Peng, S.; Oka, K.; Shibata, Y. Site Structure and Photocatalytic Role of Sulfur or Nitrogen-Doped Titanium Oxide with Uniform Mesopores under Visible Light. *J. Phys. Chem. C* **2009**, *113*, 6706–6718.

- (21) Izumi, Y.; Konishi, K.; Yoshitake, H. Specific Oxidative Dehydrogenation Reaction Mechanism over Vanadium(IV/III) Sites in TiO_2 with Uniform Mesopores under Visible Light. *Bull. Chem. Soc. Jpn.* **2008**, *81*, 1241–1249.

- (22) Masih, D.; Yoshitake, H.; Izumi, Y. Photo-oxidation of Ethanol on Mesoporous Vanadium–Titanium Oxide Catalysts and the Relation to Vanadium(IV) and (V) Sites. *Appl. Catal., A* **2007**, *325*, 276–282.

- (23) Strunk, J.; Kähler, K.; Xia, X.; Muhler, M. The Surface Chemistry of ZnO Nanoparticles Applied as Heterogeneous Catalysts in Methanol Synthesis. *Surf. Sci.* **2009**, *603*, 1776–1783.

- (24) Fujita, S.; Usui, M.; Ito, H.; Takezawa, N. Mechanisms of Methanol Synthesis from Carbon Dioxide and from Carbon Monoxide at Atmospheric Pressure over Cu/ZnO. *J. Catal.* **1995**, *157*, 403–413.

- (25) Busca, G.; Lamotte, J.; Lavalley, J. C.; Lorenzelli, V. FT-IR Study of the Adsorption and Transformation of Formaldehyde on Oxide Surfaces. *J. Am. Chem. Soc.* **1987**, *109*, 5197–5202.

- (26) Burch, R.; Golunski, S. E.; Spencer, M. S. The Role of Copper and Zinc Oxide in Methanol Synthesis Catalysts. *J. Chem. Soc., Faraday Trans.* **1990**, *86*, 2683–2691.

- (27) Chauvin, C.; Saussey, J.; Lavalley, J. C.; Idriss, H.; Hinderman, J. P.; Kinnemann, A.; Chaumette, P.; Couty, P. Combined Infrared-Spectroscopy, Chemical Trapping, and Thermoprogrammed Desorption Studies of Methanol Adsorption and Decomposition on ZnAl_2O_4 and $\text{Cu/ZnAl}_2\text{O}_4$ Catalysts. *J. Catal.* **1990**, *121*, 56–69.

- (28) Millar, G. J.; Rochester, C. H.; Waugh, K. C. Evidence for the Adsorption of Molecules at Special Sites Located at Copper-Zinc Oxide Interfaces: Part 1. A Fourier-Transform Infrared Study of Formic Acid and Formaldehyde Adsorption on Reduced and Oxidised Cu/ZnO/ SiO_2 Catalysts. *J. Chem. Soc., Faraday Trans.* **1992**, *88*, 1033–1039.

- (29) Lamberti, C.; Bordiga, S.; Salvalaggio, M.; Spoto, G.; Zecchina, A. XAFS, IR, and UV-Vis Study of the Cu^1 Environment in Cu^1 -ZSM-5. *J. Phys. Chem. B* **1997**, *101*, 344–360.

(30) Solomon, E. I.; Jones, P. M.; May, J. A. Electronic Structures of Active Sites on Metal Oxide Surfaces: Definition of the Copper-Zinc Oxide Methanol Synthesis Catalyst by Photoelectron Spectroscopy. *Chem. Rev.* **1993**, *93*, 2623–2644.

(31) Izumi, Y.; Nagamori, H. Site-Selective X-Ray Absorption Fine Structure (XAFS) Spectroscopy (2). XAFS Spectra Tuned to Surface Active Sites of Cu/ZnO and Cr/SiO₂ Catalysts. *Bull. Chem. Soc. Jpn.* **2000**, *73*, 1581–1587.

(32) Lin, K. S.; Pan, C. Y.; Chowdhury, S.; Lu, W.; Yeh, C. T. Synthesis and Characterization of CuO/ZnO-Al₂O₃ Catalyst Washcoat Thin Films with ZrO₂ Sols for Steam Reforming of Methanol in a Microreactor. *Thin Solid Films* **2011**, *519*, 4681–4686.

(33) Park, K.; Xi, J.; Zhang, Q.; Cao, G. Charge Transport Properties of ZnO Nanorod Aggregate Photoelectrodes for DSCs. *J. Phys. Chem. C* **2011**, *115*, 20992–20999.

(34) Li, Z.; Zhong, W.; Li, X.; Zeng, H.; Wang, G.; Wang, W.; Yang, Z.; Zhang, Y. Strong Room-Temperature Ferromagnetism of Pure ZnO Nanostructure Arrays via Colloidal Template. *J. Mater. Chem. C* **2013**, *1*, 6807–6812.

(35) Lv, Y.; Pan, C.; Ma, X.; Zong, R.; Bai, X.; Zhu, Y. Production of Visible Activity and UV Performance Enhancement of ZnO Photocatalyst via Vacuum Deoxidation. *Appl. Catal., B* **2013**, *138-139*, 26–32.

(36) Ran, F. Y.; Tanemura, M.; Hayashi, Y.; Hihara, T. Effect of Substrate Temperature on the Room-Temperature Ferromagnetism of Cu-Doped ZnO Films. *J. Cryst. Growth* **2009**, *311*, 4270–4274.

(37) Youn, S. K.; Ramgir, N.; Wang, C.; Subannajui, K.; Cimalla, V.; Zacharias, M. Catalyst-Free Growth of ZnO Nanowires Based on Topographical Confinement and Preferential Chemisorption and Their Use for Room Temperature CO Detection. *J. Phys. Chem. C* **2010**, *114*, 10092–10100.

(38) Wilmer, H.; Kurtz, M.; Klementiev, K. V.; Tkachenko, O. P.; Grünert, W.; Hinrichsen, O.; Birkner, A.; Rabe, S.; Merz, K.; Driess, M.; et al. Methanol Synthesis over ZnO: A Structure-Sensitive Reaction? *Phys. Chem. Chem. Phys.* **2003**, *5*, 4736–4742.

(39) Ohno, T.; Higo, T.; Murakami, N.; Saito, H.; Zhang, Q.; Yang, Y.; Tsubota, T. Photocatalytic Reduction of CO₂ over Exposed-Crystal-Face-Controlled TiO₂ Nanorod Having a Brookite Phase with Co-Catalyst Loading. *Appl. Catal., B* **2014**, *152-153*, 309–316.

(40) Roy, N.; Sohn, Y.; Pradhan, D. Synergy of Low-Energy {101} and High-Energy {001} TiO₂ Crystal Facets for Enhanced Photocatalysis. *ACS Nano* **2013**, *7*, 2532–2540.

(41) Yu, J.; Low, J.; Xiao, W.; Zhou, P.; Jaroniec, M. Enhanced Photocatalytic CO₂-Reduction Activity of Anatase TiO₂ by Coexposed {001} and {101} Facets. *J. Am. Chem. Soc.* **2014**, *136*, 8839–8842.

(42) Polster, C. S.; Nair, H.; Baetsch, C. D. Study of Active Sites and Mechanism Responsible for Highly Selective CO Oxidation in H₂ Rich Atmospheres on a Mixed Cu and Ce Oxide Catalyst. *J. Catal.* **2009**, *266*, 308–319.

(43) Yoshida, Y.; Izumi, Y. Binary Metal (Ti, Cu) Oxyhydroxy–Organic (Terephthalate) Framework: An Interface Model Nanocatalyst for Hydrogen Purification. *J. Catal.*, revision submitted according to reviews.

(44) Lopatiuk, O.; Chernyak, L.; Osinsky, A.; Xie, J. Q.; Chow, P. P. Electron-Beam-Induced Current and Cathodoluminescence Studies of Thermally Activated Increase for Carrier Diffusion Length and Lifetime in *n*-Type ZnO. *Appl. Phys. Lett.* **2005**, *87*, 162103–1–162103–3.

(45) Soudi, A.; Dhakal, P.; Gu, Y. Diameter Dependence of the Minority Carrier Diffusion Length in Individual ZnO Nanowires. *Appl. Phys. Lett.* **2010**, *96*, 253115–1–253115–3.